



Enhanced lithiation and fracture behavior of silicon mesoscale pillars via atomic layer coatings and geometry design



J.C. Ye^a, Y.H. An^{a,c}, T.W. Heo^a, M.M. Biener^a, R.J. Nikolic^b, M. Tang^a, H. Jiang^c,
Y.M. Wang^{a,*}

^a Physical and Life Sciences Directorate, Lawrence Livermore National Laboratory, Livermore, CA 94550, USA

^b Center for Micro and Nano Technology, Lawrence Livermore National Laboratory, Livermore, CA 94550, USA

^c School for Engineering of Matter Transport and Energy, Arizona State University, Tempe, AZ 85287, USA

HIGHLIGHTS

- Atomic layer deposition (ALD) of metal oxides is found to enhance the Li transport.
- The volume expansion and fracture of silicon micropillars are improved by ALD.
- Square geometry is more beneficial for large lithium storage without fracture.
- Extrapolation of anisotropic behavior from nano- to micro-sized region is cautioned.
- Models are developed to address expansion behavior of silicon micropillars after ALD.

ARTICLE INFO

Article history:

Received 18 August 2013

Received in revised form

20 September 2013

Accepted 23 September 2013

Available online 3 October 2013

Keywords:

Lithium ion battery

Silicon micropillars

Atomic layer deposition

TiO₂

Al₂O₃

Fast lithium ion transport

ABSTRACT

Crystalline silicon nanostructures are commonly known to exhibit anisotropic expansion behavior during the lithiation that leads to grooving and fracture. Here we report surprisingly relatively uniform volume expansion behavior of large aspect-ratio (~ 25), well-patterned, n-type (100) silicon micropillars ($\sim 2 \mu\text{m}$ diameter) during the initial lithiation. The comparison results with and without atomic layer metal oxides (Al₂O₃ and TiO₂) coatings reveal drastically enhanced solid electrolyte interphase (SEI) formation, higher volume expansion, and increased anisotropy. Square-pillars are found to exhibit nearly twice volume expansion without fracture compared to circular-pillars. Models are invoked to qualitatively address these beneficial or detrimental properties of silicon for lithium ion battery. Our experiments and computer simulations point at the critical relevance of SEI and pristine geometry in regulating volume expansion and failure. ALD-coated ultrathin metal oxides can act as an ion channel gate that helps promote fast Li⁺ transport into the bulk by changing the surface kinetics, suggesting new ways of designing electrodes for high-performance lithium ion battery applications.

© 2013 Elsevier B.V. All rights reserved.

1. Introduction

The large lithium storage capacity ($\sim 3579 \text{ mAh g}^{-1}$) and industry scalable manufacturing capability of various silicon materials (including micro- and nano-scale structures) have inspired intense research in these materials as anodes for lithium-ion batteries (LIBs) [1,2]. The enormous potential of silicon as energy storage materials has however been counteracted by several known challenges, including a rather large volume expansion (VE $\sim 300\%$) during lithiation that inevitably degrades the structural integrity of

silicon electrodes during the cycling, highly anisotropic lithiation/delithiation behavior witnessed in single crystalline silicon, and poor solid electrolyte interphase (SEI) layer formation. To overcome the first two shortcomings, a wide variety of nanostructures or amorphous silicon (e.g., nanowires, nanotubes, nanoparticles, and nanoporous structures) have been intensively investigated where much valuable information has been garnered [3–7]. Unfortunately nanostructured silicon is expensive to scale-up and also suffers from intrinsically low tap density (leading to low volumetric capacity). Furthermore, high surface area nanostructures inevitably induce worse SEI layers that are known to degrade the performance of LIBs [8]. In comparison, the electrochemical and electromechanical behavior of mesoscale (e.g., micrometer-sized) silicon is less well understood. To date a limited amount of experiments have

* Corresponding author.

E-mail address: ymwang@llnl.gov (Y.M. Wang).

been conducted [9,10]. Because of the clear size, stress and subsequent phase boundary curvature differences, the lithiation kinetics of micro-sized silicon is expected to be different from that of nanostructures. Such information could bear critical relevance to the commercial applications due to the high energy density needs that call for thick electrodes (e.g., commercial electrodes are typically over 100 μm thick).

Another critical challenge yet little understood to the long cycle life of silicon-based LIBs is to overcome the poor SEI layers that are intrinsically associated with large volume change electrodes. Such SEI layers are unstable both mechanically and thermally as the SEI layer is an organic/inorganic composite (e.g., containing Li_2CO_3 , LiF , $(\text{CH}_2\text{OCO}_2\text{Li})_2$, polycarbonates) [8,11] that could decompose at a relatively low temperature. The continuous re-exposure of fresh silicon to electrolyte due to the instability of SEI leads to low Coulombic efficiency and may promote subsequent exothermic reactions that lead to “thermal runaway” and cause fire and explosion of LIBs due to the chain reactions of oxidative cathode materials (if a full cell configuration is used). As such, the thermal and mechanical stability of SEI layers on anodes is of importance to the safety of LIBs. To this end, few studies have been performed to address these SEI issues, with existing effort focused on carbon or silicon oxide coatings as the potential front-runner solutions. The former is electrically conductive such that it may not be able to impede the growth of SEI at low potentials [10], while the latter has low fracture toughness, Table 1 [12–18], and can be reactive to fluoride species, and thus requires strict structural designs [1]. Another important class of coating materials is metal oxides, which can not only offer high thermal stability, but also possess other beneficial properties such as high mechanical strength and fracture toughness, low electrical conductivity, and high lithium diffusivity (Table 1 [19]). These unique properties render them as excellent surface protection materials for anodes (as well as cathodes). Enhanced cycling performance and high Coulombic efficiency have indeed been reported in Al_2O_3 -coated silicon nanostructures [20,21]. Nonetheless, there exists limited understanding of the impact of metal oxide coatings on the lithiation and fracture/failure behavior of silicon materials.

By using atomic layer deposition (ALD), here we report on the substantially enhanced lithiation and fracture behavior of silicon micropillar arrays that are ALD-ed with an ultrathin layer (<1 nm) of Al_2O_3 and TiO_2 , respectively. Silicon micropillars for this study were directly fabricated from (100) n-type silicon wafers with a diameter of 2 μm and a height of 50 μm , yielding a height/diameter aspect ratio of 25:1. To our knowledge, this is the highest aspect ratio silicon micropillars reported so far for investigation of lithiation behavior, which mechanistically ensures plane strain condition near the pillar top without having to take into account the substrate confinement effect. Similar pillars have been popularly used as thermal neutron detector materials with excellent performance [22]. The penetration ability of ALD technique to very high aspect ratio structures further makes these

studies possible. We investigate two types of conformal coatings; i.e., 0.43-nm-thick Al_2O_3 and 0.75-nm-thick TiO_2 , respectively (both thicknesses are nominal). To explore the initial pillar geometry effect on the lithiation/fracture behavior, square micropillars were also fabricated. Systematic and comparison experiments were performed on the bare silicon circular micropillars (bare-Circular-Si), Al_2O_3 -coated (Al_2O_3 -ALD-Circular-Si) and TiO_2 -coated (TiO_2 -ALD-Circular-Si) silicon circular micropillars, and TiO_2 -coated square micropillars (TiO_2 -ALD-Square-Si). For the square-shaped pillars, the orientation of four sides is oriented along {110} crystallographic planes, which is considered as the fastest Li diffusion direction in silicon. Earlier studies have generally revealed that circular shape nanowires exhibit strong anisotropic expansion, leading to grooving and fracture. It is thus interesting and of technological importance whether similar behavior occurs in mesoscale pillars and whether one can take advantage of geometrical design to mitigate or even completely annihilate such anisotropic failure behavior.

2. Experimental details

2.1. Preparation of Si micropillars

Bulk n-type (100) silicon wafers with the conductivity of 2 S cm^{-1} (determined by a four point probe method) were selected for micropillar fabrication. The pillar diameter and spacing were defined lithographically, followed by inductively coupled plasma etching. The etching process used a Bosch Process (also known as pulsed or time-multiplexed etching), alternating repeatedly between two modes to achieve vertical structures. This was accomplished by alternating between isotropically etching the silicon with a short duration of 25 sccm SF_6 plasma, and a short duration of polymerization using 80 sccm C_4F_8 . The passivation layer protected the entire substrate from further chemical attack and protected further etching. Circular- and square-shaped pillars were fabricated according to the applied mask. The diameter, spacing and height of the pillars were 2 μm , 2 μm and 50 μm , respectively. The high quality and well-patterned nature of all as-fabricated pillars can be seen in Fig. 1 a–c scanning electron microscopic (SEM) images.

2.2. TiO_2 and Al_2O_3 ALD coatings

To investigate the coating effect, silicon micropillars were coated with sub-nanometer-thick Al_2O_3 or TiO_2 films using the well-established trimethyl-aluminum ($\text{AlMe}_3/\text{H}_2\text{O}$) [23] and titanium tetrachloride ($\text{TiCl}_4/\text{H}_2\text{O}$) [24] atomic layer deposition (ALD) processes in a warm wall reactor with the wall temperature of 100 $^\circ\text{C}$ and the sample stage temperature of 125 $^\circ\text{C}$ for Al_2O_3 and 110 $^\circ\text{C}$ for TiO_2 . Long pump, pulse and purge times (20 s/50 s/50 s) were used to ensure uniform coatings throughout the material. The nominal film thicknesses using 15 cycles for TiO_2 and 3 cycles for Al_2O_3 are 0.75 nm and 0.43 nm based upon the ALD rates reported in Refs. [25] and [26], respectively.

2.3. Transmission electron microscopy (TEM) sample preparation

The TEM samples of TiO_2 ALD coated silicon micropillars were prepared by using a focused-ion-beam (FIB) (FEI, Nova 600) liftout method, where the target pillar arrays were first coated with a thin protection layer of e-beam Pt, followed by the further deposition of ion-beam Pt which helps to “weld” several pillars together, Fig. 1d. The cross-sectional samples were examined in a FEG Philips CM300 TEM with traditional bright-field (BF) and high-resolution (HR) imaging conditions. The BF TEM in Fig. 1e suggests that the side

Table 1
Selected properties of silicon, SiO_2 and metal oxides.

Materials	Fracture toughness ($\text{MPa m}^{1/2}$)	Electrical conductivity (S cm^{-1})	Li ion conductivity (S cm^{-1})
Al_2O_3	2.7–4.2 [17]	10^{-14} (Crystalline) [16]	10^{-6} (Amorphous) [12]
TiO_2	2.38 [17]	10^{-6} [14]	10^{-5} to 10^{-7} (Rutile) [15]
SiO_2	0.79 [19]	10^{-14} [16]	—
Si	$<110>$: 0.73 $<100>$: 0.89 [18]	2 (Our data)	$\sim 3 \times 10^{-7}$ [13]

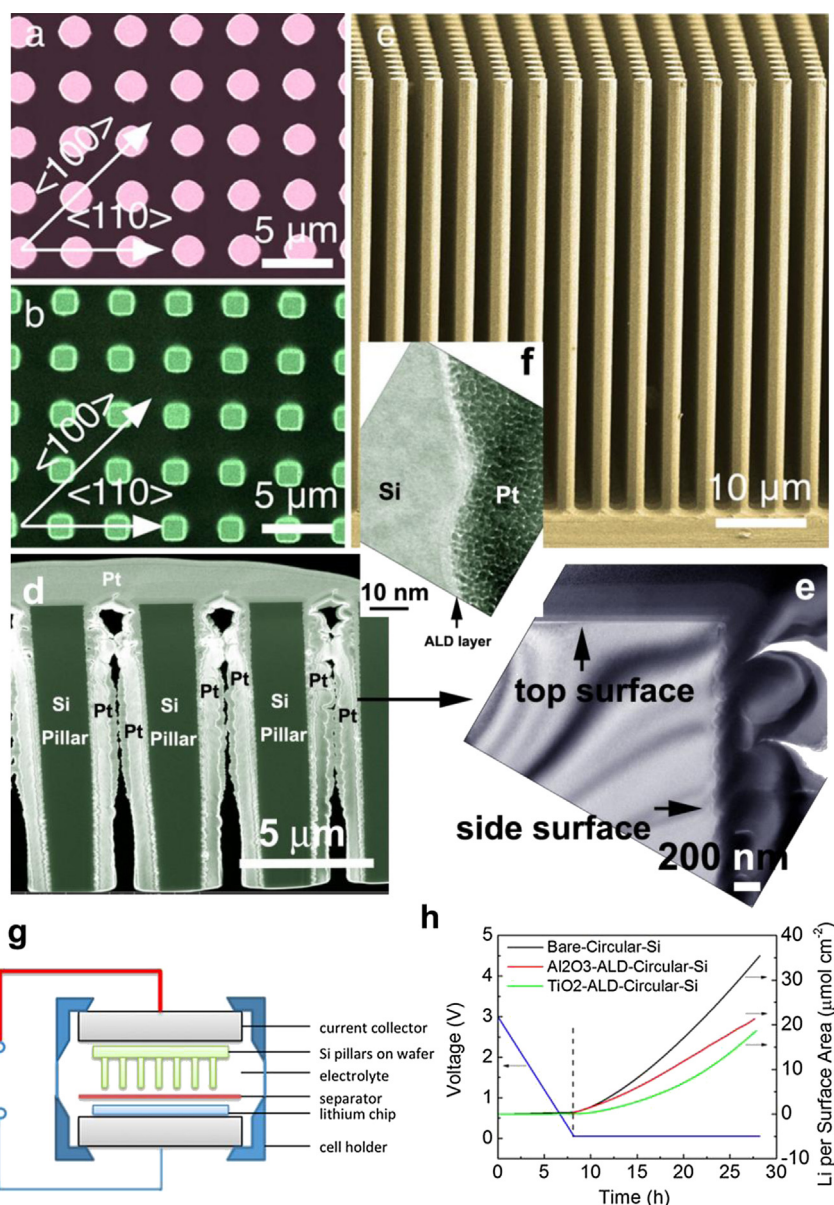


Fig. 1. (colour online) Initial morphology of silicon micropillars and the experimental setup. (a) and (b), top-view SEM image of circular and square pillars, respectively. The crystallographic orientations are labeled in the figure. (c) A side-view SEM image of circular pillars. (d) A cross-sectional SEM image of a liftout piece, showing several cut and welded silicon pillars. (e) A BF TEM image of silicon pillar with side- and top-surface marked. (f) A zoomed-in high-resolution TEM image of the side surface of silicon pillars. (g) An illustration of our experimental setup using a half-cell assembly. (h) Voltage and lithiation profile of three types of circular pillars. Note that the apparent lithiation rate of ALD-coated samples seems lower compared to the bare-Circular-Si. This phenomenon could be caused by the formation of SEI layers without ALD coatings (see text for detailed discussion).

surface of silicon pillars generally exhibit zig-zag etching features, which is in contrast to the atomic smoothness of the top surface of the pillars. The atomic coating layer of TiO_2 is generally visible in HRTEM image shown in Fig. 1f. However, the thickness of the ALD observed under TEM appears thicker than the nominal thickness of ALD layer calculated from the deposition rate of our processes, likely due to the compound effect of TEM sample thickness, tilting angles of the sample towards electron beam, and the fact that the side surface could also contain silicon native oxide layers.

2.4. Cell assembly and characterizations

The silicon micropillars standing on a Si wafer were directly assembled into a Swagelok-type half-cell ($\sim 71 \text{ mm}^2$ surface area)

with lithium metal as the counter electrode. A commercial electrolyte (MTI Cor.) of 1 M LiPF_6 in a mixed solution of ethylene carbonate, diethyl carbonate and dimethyl carbonate (EC/DEC/DMC, $v/v = 1:1:1$) was adopted with a polypropylene separator (Celgard 3501, PP double layer, $\sim 25 \mu\text{m}$ each). Cell assembly was completed in an argon-filled glove box (VAC Omni) with oxygen and water content less than 1 ppm. A Maccor 4304 battery cycler was used to perform the initial lithiation process from the open circuit potential ($\sim 3 \text{ V}$) to a target voltage of 50 mV at a constant scan rate of 0.1 mV s^{-1} , and then was held for 20 h. After electrochemical lithiation, cells were disassembled inside the glove box and the lithiated electrodes were washed by dimethyl carbonate (DMC) for imaging. The morphology change was characterized by a field-emission scanning electron microscope (SEM, JEOL 7401-F)

operated at 2 kV. The same FIB machine was used to cross section some selected pillars for SEI examinations.

3. Experimental results and discussion

3.1. Unexpected lithiation behavior before and after ALD

With a half-cell configuration shown in Fig. 1g, we investigated the initial lithiation behavior of above silicon micropillars, including Li uptake, SEI formation, VE, and fracture behavior. The lithiation time for all pillars is fixed at 20 h, and the total Li uptake is estimated from the current profile for three types of circular pillars, as illustrated in Fig. 1h. By using the data in the figure, and assuming that the Li intake is mainly due to the silicon micropillars, we found that the apparent lithiation intake of bare Si can reach up to 8.8 Li per Si after 20 h of lithiation, which is well above the theoretical Li storage capacity (3.75 Li per Si by assuming $\text{Li}_{15}\text{Si}_4$ room-temperature product). Such a crude estimation however did not take into account of the potential current leakage and the lithium intake of the substrate. Nonetheless, this could also suggest the formation of massive SEI layers under the current low-voltage lithiation conditions (i.e., 50 mV). This SEI behavior is confirmed by SEM images shown in Fig. 2a, where the SEI layer appears rather rough for the bare silicon. In contrast, such SEI formation has been substantially mitigated in both Al_2O_3 -coated and TiO_2 -coated samples, Fig. 2b and c, respectively. The contrast behavior of SEI formation for bare silicon and ALD-coated samples can be better viewed from the side surface for all three samples, Fig. 3. Quantitative measurements of SEI for bare silicon reveal a thickness of up to $\sim 0.5\text{--}0.8\ \mu\text{m}$ (Fig. 3a), whereas the thickness of SEI layer in ALD-coated samples is no more than 150 nm, as indicated by the FIB cutting image shown in Fig. 3e. Unexpectedly, we observe relatively uniform VE behavior for the bare-Circular-Si before the fracture (Figs. 2a and 3a), in contrast to widely reported anisotropic expansion of silicon crystalline nanowires or nanopillars [3]. In our cases, strong anisotropic expansion is only observed for ALD-coated samples (Fig. 2b and c). The near uniform expansion behavior seen

in the bare-Circular-Si suggests that the formation of SEI layers plays a crucial role in regulating lithium transport under the current experimental conditions, and that the lithiation behavior of these bare-Circular-Si micropillars may no longer be controlled by the phase-boundary mobility [2]. To quantify the anisotropic VE behavior in three types of samples, we define an anisotropic index factor χ as the ratio of pillar dimension along the $\langle 110 \rangle$ ($d_{\langle 110 \rangle}$, preferentially swelling direction) and $\langle 100 \rangle$ direction ($d_{\langle 100 \rangle}$, less expansion direction) right before the crack formation. Table 2 indicates that the bare-Circular-Si has a χ value of 1.02 ± 0.03 (i.e., near uniform expansion), approximately 13% smaller compared to the values of Al_2O_3 -ALD-Circular-Si ($\chi = 1.15 \pm 0.03$) and TiO_2 -ALD-Circular-Si ($\chi = 1.13 \pm 0.04$) pillars. Moreover, we find that the overall achievable VE before fracture of both ALD-samples is about 10% higher than that of the bare-Circular-Si, suggesting the positive role of ALD coatings. The χ values measured in both ALD-samples suggest that the lithiation rate along [110] and [100] orientations is on average $\sim 15\%$ – a value that seems substantially smaller than that reported in the literature [2,9]. The present experimental results also indicate that, due to the excellent ionic conductivity but electronically insulating nature of metal oxides (see Table 1), these ultrathin ALD coatings not only help to form and stabilize thin SEI layers (leakage of electrons is one of the main causes that promote the decomposition of electrolytes), but also enhance the VE of silicon micropillars (likely due to the suppression of surface defects after ALD, to be discussed later).

3.2. Square pillars vs. circular pillars (geometry effect)

Compared to circular pillars, the VE behavior of square pillars is quite intriguing. For meaningful comparison, we also ALD-ed square pillars with the same thickness of TiO_2 and carried out lithiation experiments under the same conditions as those of circular pillars. Interestingly, the square pillars become near circular shape after lithiation due to the preferential expansion of {110} side surface, Fig. 2d. As a result, the χ value increases from 0.71 (square) to 0.95 ± 0.02 (close to circular shape) after lithiation. Significantly,

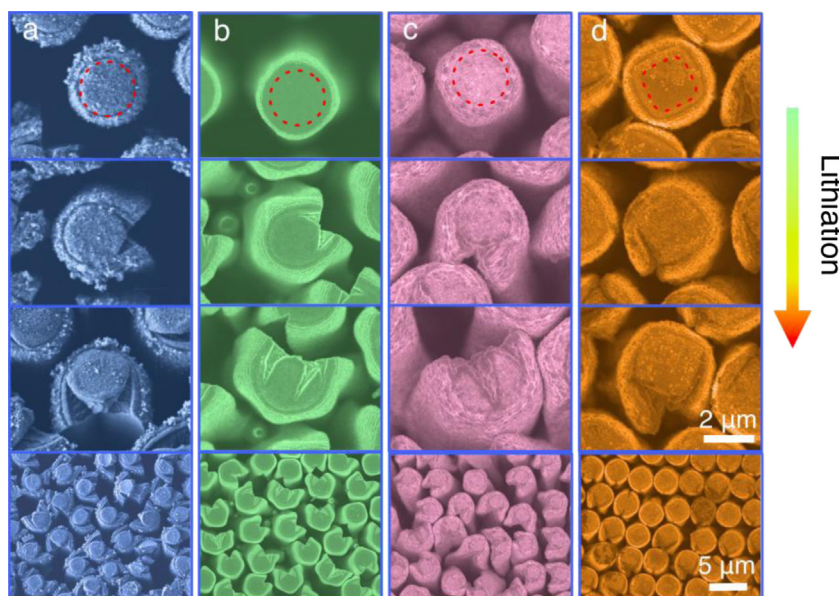


Fig. 2. Cross-sectional morphology evolutions during the progressive lithiation for four types of silicon pillars: (a) bare-Circular-Si, (b) Al_2O_3 -ALD-Circular-Si, (c) TiO_2 -ALD-Circular-Si, and (d) TiO_2 -ALD-Square-Si. The red dashed lines in the first row denote the original size and shape of the respective pillars. The bottom row is the low magnification images of various pillars. The scale bar is the first three rows is $2\ \mu\text{m}$, and the last row is $5\ \mu\text{m}$. Note the very different shape change and fracture patterns/directions in these pillars. (For interpretation of the references to colour in this figure legend, the reader is referred to the web version of this article.)

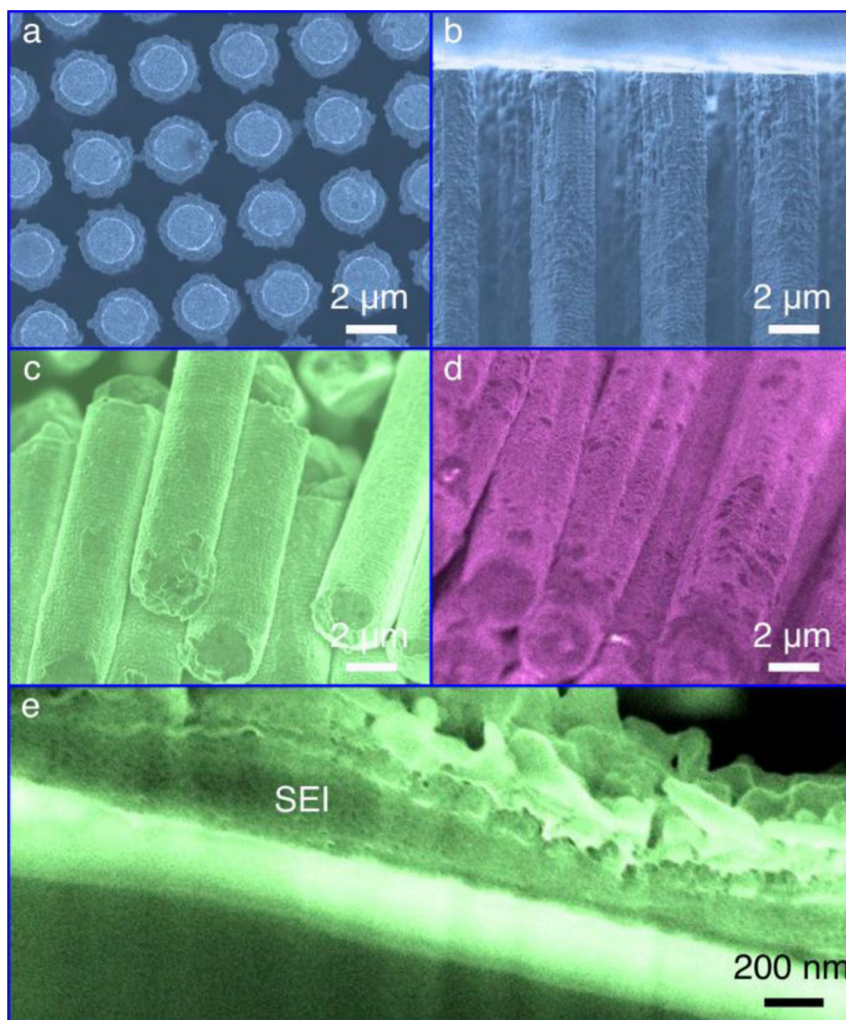


Fig. 3. Formation of SEI in three types of circular pillars. (a) top- and (b) side-view of bare silicon after partial lithiation. Note the thick SEI layers observable from (a). (c) and (d) Side-view of Al_2O_3 -ALD-Circular-Si and TiO_2 -ALD-Circular-Si after partial lithiation. Note the smooth and clean nature of these surfaces. (e) Focused-ion-beam (FIB) cross-sectional cutting of Al_2O_3 -ALD-Circular-Si sample after partial lithiation. Note that the sample has been exposed to the air for a few hours before the FIB sectioning, which may have increased the surface roughness of the SEI layer.

the overall VE of square pillars increases up to 165% before cracks initiate; this represents an impressive 87.5% increment over the circular pillars, Table 2. These results strongly argue that square shape (instead of circular one) is a better geometry for large Li storage in silicon – an interesting observation that has not been reported in the literature.

3.3. Fracture behavior

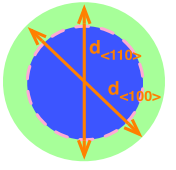
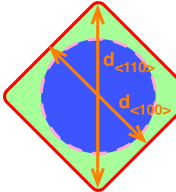
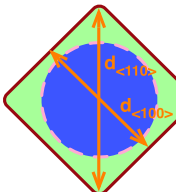
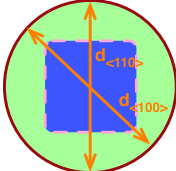
It is noted in Fig. 2a–c that all silicon pillars exhibit popcorn type fracture patterns, where cracks appear to initiate from the out surface of circular pillars, penetrating into the crystalline core and also propagating along the crystalline-amorphous interfaces. In addition, all pillars (including square ones) seem to fail from one major crack rather than multiple ones. To obtain more quantitative information, we have measured the crack orientations of all four types of silicon pillars. Fig. 4 illustrates the statistical crack orientation information for the bare-Circular-Si, ALD circular pillars (both), and TiO_2 -ALD-square-Si. Due to the relatively uniform expansion behavior of the bare-Circular-Si, we observe that the crack orientation of these samples is somewhat stochastic with slight preference along $\langle 110 \rangle$ direction, Fig. 4a; i.e., the reported preferential fracture oriented 45° to $\langle 110 \rangle$ direction for (100)-type

silicon nanopillars is not observed in our micropillars [3]. For ALD circular pillars, cracks seem to initiate unanimously along $\langle 110 \rangle$ direction (i.e., the most swelling direction), Fig. 4b, whereas for ALD square pillars, along $\langle 100 \rangle$ direction (i.e. one corner of the square), Fig. 4c. These fracture orientations are not only drastically different from those of our own bare silicon, but also differ from dominant fracture orientations reported so far in the literature [3], suggesting that the fracture process in silicon micropillars can be quite a complex, which seems affected by the sample size, initial geometry, surface coatings/defects, or even dopant type. In addition, different electrochemical reaction rate used in various experiments could also play a significant role. Note that the different fracture orientations reported in the literature are mainly observed in p-type silicon nanopillars [3], whereas our samples are n-type pillars. Furthermore, there are clear sample size and lithiation condition differences. The experimental results here underscore the importance of taking into account the strong size effect, initial sample geometry, and electrochemical cycling conditions when designing silicon anode structures for LIBs.

To further grip the crack growth trends for all four types of pillars studied, we measured the crack length (L) (defined in Fig. 5a, where R is the original radius of the pillar) vs. VE for a number of randomly selected pillars. The results are summarized in Fig. 5b for

Table 2

Anisotropic shape index before (χ_{before}) and after (χ_{after}) lithiation for various silicon pillars, which is defined as the ratio of dimension along $\langle 110 \rangle$ and $\langle 100 \rangle$ directions: $\chi = d_{\langle 110 \rangle} / d_{\langle 100 \rangle}$. χ_{after} is measured at ΔV_c (the maximum volume expansion before the crack formation).

Pillar type	Geometry	χ_{before}	χ_{after}	Average lithiation velocity difference along $\langle 110 \rangle$ and $\langle 100 \rangle$
Bare-circular-Si		1	1.02 ± 0.03 @ ~ 0	$\Delta V_c = 82\%$
Al ₂ O ₃ -ALD-circular-Si		1	1.15 ± 0.03 @ $\sim 15\%$	$\Delta V_c = 92\%$
TiO ₂ -ALD-circular-Si		1	1.13 ± 0.04 @ $\sim 13\%$	$\Delta V_c = 88\%$
TiO ₂ -ALD-square-Si		0.71	0.95 ± 0.02 @ $-$	$\Delta V_c = 165\%$

all pillars. In the figure, one could gauge the easiness of the crack propagation through examining the slope (K) of L/R vs. VE. A larger K would mean that the crack is prone to propagation under the same VE. We note that, for the bare silicon, the cracks always nucleate from the out surface after a VE of less than 100% and start to grow inwards with a K value of ~ 2.7 . Both ALD-coated samples follow a similar trend ($K \sim 2.3$) but with a slightly larger x -axis offset compared to the bare silicon, suggesting that ALD coating might have helped to arrest the crack nucleation. We speculate that

as our coating thickness is no more than 1 nm (i.e., negligibly thin compared to the sample dimension), the possible mechanical constraint effect is insignificant. This is consistent with similar K values observed for all three circular-shape samples. As mentioned above and indicated in Fig. 5b, the ALD-square pillars reveal a critical VE of 165% that is much larger than the circular ones. This implies a strong delay of crack nucleation and propagation. In addition, we find a K value of ~ 1.5 for these square pillars, which is also substantially smaller than those of circular ones (2.3–2.7), testifying more difficult event of crack propagation in the square pillars. Based upon the critical VE without fracture (ΔV_c), one can estimate a reversible capacity of $\sim 2300 \text{ mAh g}^{-1}$ for ALD square pillars, in contrast to a much smaller capacity of $\sim 1400 \text{ mAh g}^{-1}$ for circular pillars.

Another important question pertaining to the crack propagation is whether the two phase boundary can effectively divert or obstruct the crack propagation. If this occurs, one would expect to see the crack length (L) equal or be smaller than the amorphous shell thickness (t ; i.e., lithiated area). Assuming the isotropic VE (ΔV), one can estimate t/R from the total ΔV as:

$$t/R = \sqrt{1 + \Delta V} - \sqrt{1 - \Delta V / \Delta V_t} \quad (1)$$

where ΔV_t represents the theoretical VE of silicon. The calculated t/R trend follows the dashed line shown in Fig. 5b. Evidently, L/R values surpass the t/R line for all three circular pillars when the VE is above $\sim 100\%$, suggesting that the cracks propagate well into the crystalline silicon core for circular pillars, consistent with the SEM image shown in Fig. 5a. In contrast, this behavior is not seen for square pillars, which again suggests the difficult event of crack propagation in square geometry. The contrast results between circular and square pillars promote us to argue that the stress state/distribution in these two types of pillars could be very different.

4. Theoretical framework

To understand qualitatively the effect of ALD coating and initial geometry on the VE and stress evolution of silicon micropillars upon lithiation, a two-phase model is developed, following the literature [27,28]. The model assumes that the rate-limiting processes during the lithiation involve the bulk diffusion of lithium ion through the pillars and the solid state reaction at the interface (i.e., other rate-controlling mechanisms such as surface kinetics are not considered [29,30]). As all micropillars used in our experiments have very large aspect ratio (25:1), the effect of the pillar height is negligible; that is, a cross-section representation is sufficient to portray the VE behavior, the Cartesian coordinate setup of which can be seen in the inset of Fig. 6a, with the origin coinciding with the geometric center of the cross-section and two axes along $\langle 110 \rangle$ directions. Coordinates (x, y) and angle θ are used to specify positions and directions. For the reaction controlled interface

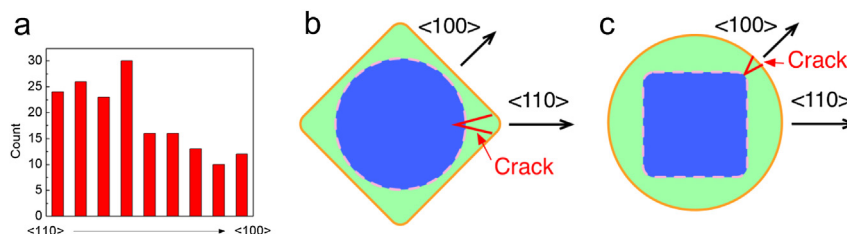


Fig. 4. (colour online) Crack orientations for three types of silicon pillars: (a) bare-Circular-Si, (b) ALD-Circular-Si (for both Al₂O₃ and TiO₂ coated), and (c) TiO₂-ALD-Square-Si. Note that all ALD-coated pillars ubiquitously fail along one orientation [either $\langle 110 \rangle$ in (b), or $\langle 100 \rangle$ in (c)], in contrast to the relatively random failure direction of bare silicon sample in (a).

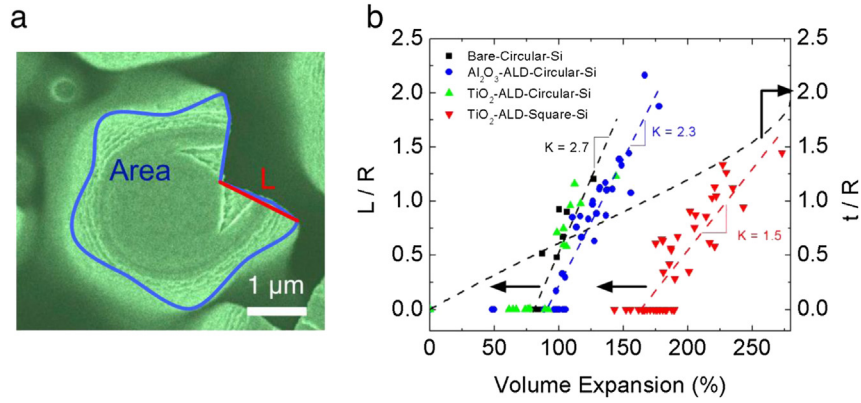


Fig. 5. (colour online) Crack nucleation and growth behavior in four types of silicon pillars. (a) The definition of L (crack length) and R (original pillar radius). The ΔV is measured by the change of pillar area on top-view using the ImageJ software. The amorphous shell thickness t is estimated according to Eqn. (1) in the main text. (b) The distribution of L/R (y1-axis) and t/R (y2-axis) as a function of the VE. Three L/R dashed lines are the least-squares-fitting of the experimental data with the slope (K) marked in the figure.

motion, interface velocity [30] is determined by $v(\theta) = \lambda_m R_j$, where λ_m is the molar volume of crystalline silicon and $R_j = \kappa(\theta)f(c_{Li}, c_{Si}, c_{Li-Si})$ is the rate of chemical reaction [here $\kappa(\theta)$ is the orientation dependent rate constant for solid state chemical reaction, and the function $f(c_{Li}, c_{Si}, c_{Li-Si})$ describes the reaction rate which is a function of the concentrations of products and reactants]. Lithium concentration is assumed saturated in the amorphous phase and zero in the crystalline phase. Thus, function

$f(c_{Li}, c_{Si}, c_{Li-Si})$ becomes a constant at the phase interface. Given the four fold symmetry of the crystal structure in the cross-section, the interface velocity can be described as

$$V(\theta) = 1/2(V_{110} + V_{100}) + 1/2(V_{110} - V_{100})\cos(4\theta). \quad (2)$$

Here $v_{110} = \lambda_m \kappa(0)$ and $v_{100} = \lambda_m \kappa(\pi/4)$ are the interface velocities at [110] and [100] orientations, respectively.

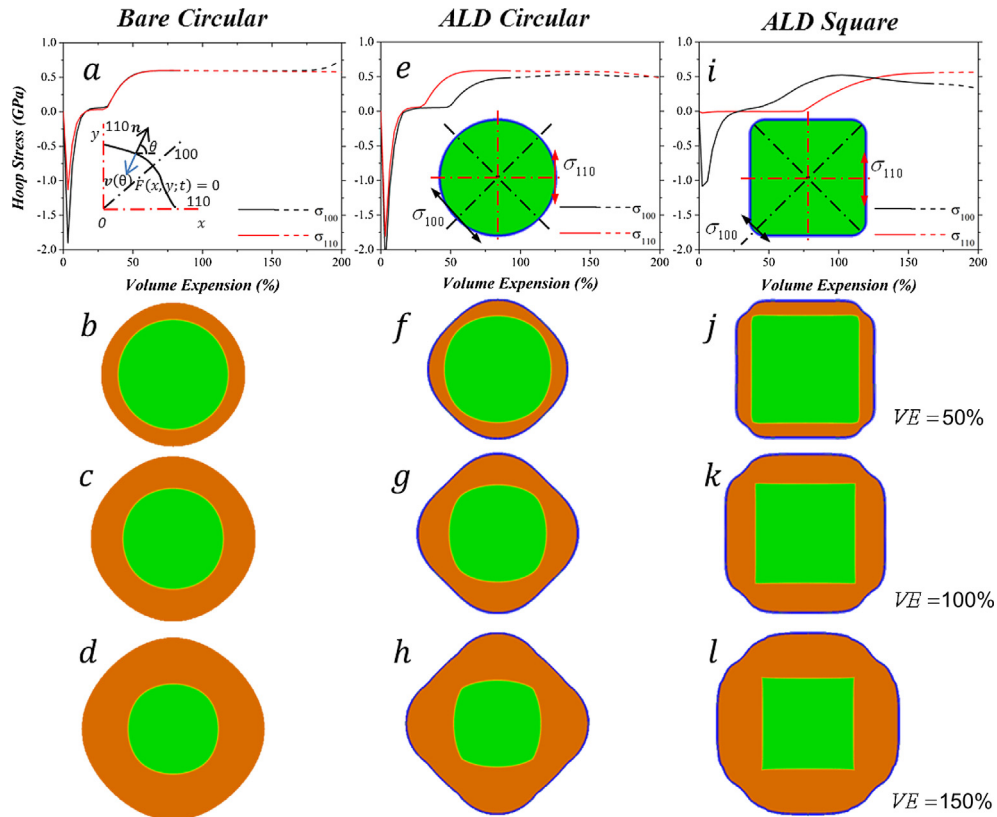


Fig. 6. Finite element simulation results for (a–d) bare-Circular-Si, (e–h) ALD-coated circular pillars, and (i–l) ALD-coated square pillars. (a) Hoop stress as a function of VE at the surface of the bare-Circular-Si perpendicular to $\langle 100 \rangle$ (black line) and $\langle 110 \rangle$ (red line) directions, respectively. The inset is the coordinate setup for simulations. (b–d). The shape change in cross-section of the bare-Circular-Si, with crystalline Si in green and amorphous Li–Si in orange at different VE of 50%, 100%, 150%, respectively. The definition of hoop stress and shape change in (e–h) and (i–l) follows the same order as the bare-Circular-Si. Note the rather anisotropic expansion behavior after ALD-coating for circular pillars (f–h), and the near circle-like expansion behavior of the square pillars (j–l). The ALD thin coating in (f–h) and (j–l) is represented by the blue solid line. (For interpretation of the references to colour in this figure legend, the reader is referred to the web version of this article.)

A large deformation method is used in our modeling [31]. The multiplicative decomposition of deformation is assumed so that the total deformation λ_i can be decomposed into three parts, namely, elastic deformation λ_i^e , plastic deformation λ_i^p , and compositional deformation λ_i^c as $\lambda_i = \lambda_i^e \lambda_i^p \lambda_i^c$ ($i = 1, 2, 3$ denotes three principal directions). The compositional strain is given by $\lambda_i^c(x, y; t) = 1 + \beta c(x, y; t)$, with $c(x, y; t)$ as the normalized lithium concentration, and β as the coefficient of compositional expansion. Elastic and plastic deformation is partitioned by the specific material law. Crystalline silicon is modeled as a cubic elastic material; amorphous Li–Si alloy and ALD coatings are both modeled as isotropic perfectly elastic–plastic materials. The von Mises yielding criterion and the associated flow rules are used to describe the plastic behavior of amorphous materials. Detailed formulation of equilibrium, compatibility, and constitutional models are available in the reference [31].

The model described above is implemented using the finite element package ABAQUS and two user-subroutines. We draw an analogy between concentration c in our problem and temperature in thermal analysis in ABAQUS. Therefore, a user subroutine UTEMP (user defined temperature) is used to evolve the interface according to the above equation with concentration $c = 1$ assigned to the amorphous phase and $c = 0$ to the crystalline phase. Another user subroutine UEXPAN is used to compute the compositional expansion based on the concentration field obtained from UTEMP, under rigorous finite deformation formulation. $\beta = 0.5874$ is used to realize the 300% VE, as $(1 + \beta)^3 = 1 + 300\%$. The field of compositional strain is passed into ABAQUS main program as the load to deform the electrode.

Table 3 lists the mechanical properties of materials involved in simulations. For ALD coatings, we choose Young's modulus $E = 150$ GPa, yield strength $\sigma_y = 2.7$ GPa [32,33], and Poisson's ratio $\nu = 0.25$ as protocol values. For (100) crystalline silicon, $E = 130$ GPa, Shear modulus $G = 79.6$ GPa, and $\nu = 0.28$ [34,35]. For Si–Li amorphous phase, we choose $E = 12$ GPa, $\sigma_y = 0.5$ – 1.0 GPa [36,37], and $\nu = 0.28$. All length quantities in the simulations are normalized by $a = 1000$ nm, which is the experimental radius for circular pillar and half-width of square pillar. $\tau = a/v_{110}$ is the time scale of full lithiation; thus time is normalized by τ and velocity is normalized by τ/a , i.e., $\bar{v}_{110} = v_{110}\tau/a$, $\bar{v}_{100} = v_{100}\tau/a$. For bare and ALD-coated pillars, the same velocity in 110 orientation was used as $\bar{v}_{110} = 1$ while different values $\bar{v}_{100} = 0.9$ and $\bar{v}_{100} = 0.6$ were used respectively to recognize the different levels of the anisotropy in these two kinds of samples; i.e., the different rate-limiting mechanisms are represented in the model by controlling the levels of reaction front velocity anisotropy for simplicity. ALD coating was modeled as a thin layer of material with a normalized thickness of 0.005.

5. Modeling results and discussion

The key purpose of this phenomenological model is to help understand very different fracture behavior observed with and without ALD coatings, and the strong sample geometry effect observed in our work. Note that earlier in-situ TEM experiments

revealed a strong orientation-dependent interface mobility during lithiation of silicon nanowires [2,38], which has been the basis of many existing modeling effort [38,39]. Our experiments here on the bare silicon pillars however indicate that the lithiation behavior of silicon materials is strongly influenced by the formation of SEI layers, which regulates/limits the lithium ion transport such that the interface mobility could become less relevant. In fact and as indicated by the modeling results shown in Fig. 6a–l, a relatively uniform VE behavior is obtained when the interface velocity difference is less than 10% along the $\langle 110 \rangle$ and $\langle 100 \rangle$ directions; i.e., the rate controlling mechanism in our bare silicon micropillars is likely to be the diffusion of lithium ion into the reaction front. Under these conditions, our simulations indicate that the corresponding hoop stresses (Fig. 6a) along $\langle 110 \rangle$ (σ_{110}) and $\langle 100 \rangle$ (σ_{100}) directions are initially compressive but quickly turn over to the positive territory (i.e., tensile). Right before the fracture (i.e., at the VE $\sim 82\%$), both stresses are clearly tensile and exhibit essentially the same values. These results agree quantitatively with relatively stochastic fracture orientations of bare silicon micropillars observed in our experiments. In contrast, an obviously anisotropic VE behavior is duplicated when the solid state reaction is assumed to control the VE behavior of ALD samples, Fig. 6e–l. Under this scenario, the hoop stresses go through a similar transition from compressive to tensile with the major difference that the hoop stress along $\langle 110 \rangle$ direction (i.e., σ_{110}) is appreciably higher than σ_{100} , leading to preferential fracture of these pillars long $\langle 110 \rangle$ orientation (as observed in our experiments).

Interestingly, the round shape expansion behavior of ALD square pillars is also reproduced when the solid state reaction is assumed to control the lithiation behavior of these pillars, the hoop stresses of which exhibit a cross-over behavior between $\langle 100 \rangle$ and $\langle 110 \rangle$ orientations. The hoop stress along $\langle 100 \rangle$ orientation is observed to be higher when the VE is less than $\sim 125\%$, which is gradually overtaken by the stress along $\langle 110 \rangle$ direction. The gradual decrease of σ_{100} as VE increases is observed to be linked with the stress relaxation along the corner of the square (Fig. 6i), suggesting that the square pillars has the ability to homogenize the stress distribution and slow down the crack nucleation or growth. The final fracture of these pillars along $\langle 100 \rangle$ direction seems pertaining to the groove development observed in our simulations, Fig. 6j–l. Note that the fracture toughness in bulk silicon is orientation dependent, with the value along $\langle 110 \rangle$ direction slightly lower than that of $\langle 100 \rangle$ direction (Table 1). This small fracture toughness discrepancy however does not seem to affect the fracture orientation of square pillars. The rather complex stress evolution and much larger achievable VE in these pillars suggest that square geometry can be more desirable for applications in LIBs. It is further suggested that investigations of other geometry pillars are useful in order to fully understand the initial geometric effect of silicon crystalline materials upon lithiation behavior.

Although our models have not taken into account the change of the reaction-front velocity due to the development of compressive/tensile stresses and the effect of stress on diffusivity (which might influence the interface migration kinetics), our hydrostatic stress analysis of two different selected positions located at the trajectories (along $\langle 100 \rangle$ and $\langle 110 \rangle$ orientations) of the migrating reaction front interface shown in Fig. 7 indicates the development of tensile hydrostatic stress inside crystalline core along the [100] direction in both ALD-samples (see point B2 and B3 in Fig. 7) when the reaction front propagates, suggesting the possible speedup of reaction front velocity in that orientation – a behavior that seems to contrast with some reports in nanosized silicon (e.g., nanoparticles or nanowires) [40–42]. This could have several important implications for silicon micropillars compared to nanopillars. First, the reaction front velocity change seems to help promote less

Table 3
Representative mechanical properties of some relevant materials used in simulations.

Materials	Mechanical properties
Amorphous TiO ₂	$E = 65$ – 147 GPa [33]
Amorphous Al ₂ O ₃	$E = 150$ – 155 GPa, $\sigma_y = 2.7$ GPa [32]
Amorphous Li ₁₅ Si ₄	$E = 12$ GPa, $\sigma_y = 0.5$ – 1.0 GPa [36,37]
Single crystalline Si (100)	$E = 130$ GPa, $G = 79.6$ GPa, $\nu = 0.28$ [34,35]

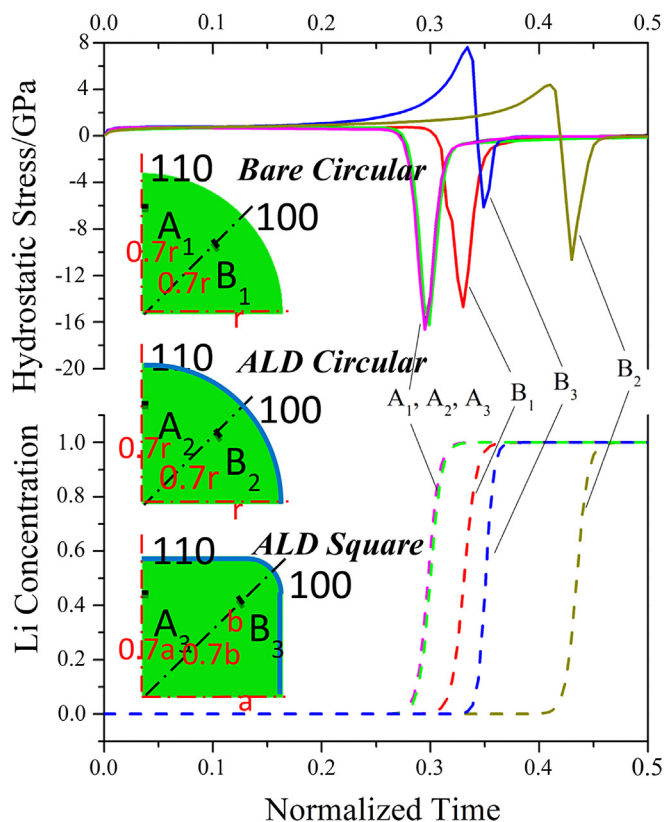


Fig. 7. (colour online) The hydrostatic stress distribution of two selected points for three types of silicon pillars. The reaction front propagation can be viewed from the Li concentration profile corresponding to each position (i.e., $A_1, A_2, A_3, B_1, B_2, B_3$). Note the development of tensile hydrostatic stress at point B_2 and B_3 as the reaction front propagates.

anisotropic expansion due to the reason mentioned above (i.e., the speedup tendency along $[100]$ orientation). Second, the effect of hydrostatic compression on diffusivity stemming from the curvature of the reaction front interface could be less significant in micropillars due to the relatively low curvature of micro-sized pillars [41]. The relatively fast lithiation in the late stage of holding time seen in Fig. 1h appears consistent with this speculation. Note however that this type of accelerated lithiation processes could also be caused by the fracture of silicon pillars, leading to the relaxation of stresses and fresh free surface for fast surface lithium diffusion and continuous lithiation. Third, due to the much large dimensions associated with micropillars (compared to nanopillars), it is conceivable that diffusion controlled processes is expected to play more significant roles in the late stage of lithiation in micropillars, which could lead to less anisotropic expansion behavior. This seems to be true in both bare- and ALD-coated-samples where less anisotropy is observed compared to those reported in silicon nanopillars. In essence, the lithiation kinetics of silicon micropillars could be very different from those of silicon nanopillars. Because of above reasons, our model assumption of different levels of reaction front velocity anisotropy for different controlling mechanisms, i.e., less anisotropic velocity for the diffusion-controlled mechanism and more anisotropic velocity for the reaction-controlled mechanism, and constant reaction front velocity seems reasonable to capture the essences of shape change of all three types of pillars, as well as the fracture orientations even though the time-dependent variation of the reaction front velocity in the case of the diffusion-controlled mechanism is not considered. We observe different rate controlling mechanisms in bare and ALD pillars, with

very different hoop stress development that is closely related to the shape of the pillars. One additional point that is worth pointing out is most existing models do not account for crystallographic orientation dependent velocity change due to the different stresses development along different orientations, which could lead to less/more velocity discrepancy in $[110]$ and $[100]$ orientations. More complete models that can account for all above factors are clearly needed in the future in order to fully address the rather complicated lithiation behavior seen in micro-sized silicon pillars.

6. Conclusions and outlook

In summary, we have investigated the initial lithiation behavior of (100) n-type silicon micropillars in three different forms: bare circular silicon, ALD-coated circular silicon, and ALD-coated square silicon pillars. In contrast to what has been reported in the literature on nanostructures, the bare silicon micropillars studied here exhibit a relatively uniform VE behavior before fracturing along somewhat stochastic directions, likely due to the regulation effect of SEI layers in controlling lithium ion flux. ALD coating of metal oxides (Al_2O_3 and TiO_2) help to form thin SEI layers, enhance surface kinetics and facilitate lithium transportation, leading to a strong anisotropic VE behavior. With or without ALD coatings, the critical VE before fracture for all circular pillars reaches up to $\sim 100\%$. With a further square-shaped geometry design, however, a critical VE of more than 165% can be reached, helped by the stress relaxation mechanisms around the corners of squares. Models are developed that are able to rationalize the overall VE and fracture behavior of all pillars. Simulations further suggest that stress distributions in various pillars may play significant roles in the fracture behavior. These findings underscore the critical importance of SEI formation in regulating the transport and eventual failure mechanisms of various pillars. ALD-coated metal oxides can act as a gate that promotes fast Li-ion diffusion into the bulk electrode through changing the surface kinetics. Questions remain what the optimized thickness of these ALD coatings would be in order to maximize Li-ion transport yet help maintain the integrity of the electrodes. Nonetheless, our results offer new insights in designing silicon-based electrodes for high energy density and high-power density electrochemical energy storage.

Acknowledgments

The authors would like to thank C.E. Reinhardt and N. Teslich for experimental assistance. Helpful discussions with B.C. Wood, J. Lee and M.D. Merrill are acknowledged. The work was performed under the auspices of the US Department of Energy by LLNL under contract No. DE-AC52-07NA27344. The project is supported by the Laboratory Directed Research and Development (LDRD) programs of LLNL (12-ERD-053 and 13-LW-031). HJ acknowledges the support from NSF CMMI-1067947 and CMMI-1162619.

References

- [1] H. Wu, G. Chan, J.W. Choi, I. Ryu, Y. Yao, M.T. McDowell, S.W. Lee, A. Jackson, Y. Yang, L.B. Hu, Y. Cui, *Nat. Nanotech.* 7 (2012) 309–314.
- [2] X.H. Liu, J.W. Wang, S. Huang, F.F. Fan, X. Huang, Y. Liu, S. Krylyuk, J. Yoo, S.A. Dayeh, A.V. Davydov, S.X. Mao, S.T. Picraux, S.L. Zhang, J. Li, T. Zhu, J.Y. Huang, *Nat. Nanotech.* 7 (2012) 749–756.
- [3] S.W. Lee, M.T. McDowell, L.A. Berla, W.D. Nix, Y. Cui, *Proc. Natl. Acad. Sci. USA* 109 (2012) 4080–4085.
- [4] C.J. Yu, X. Li, T. Ma, J.P. Rong, R.J. Zhang, J. Shaffer, Y.H. An, Q. Liu, B.Q. Wei, H.Q. Jiang, *Adv. Energy Mater.* 2 (2012) 68–73.
- [5] J.W. Wang, Y. He, F.F. Fan, X.H. Liu, S.M. Xia, Y. Liu, C.T. Harris, H. Li, J.Y. Huang, S.X. Mao, T. Zhu, *Nano Lett.* 13 (2013) 709–715.
- [6] X. Xiao, P. Liu, M.W. Verbrugge, H. Haftbaradaran, H. Gao, *J. Power Sources* 196 (2011) 1409–1416.

- [7] Y. He, X.Q. Yu, G. Li, R. Wang, H. Li, Y.L. Wang, H.J. Gao, X.J. Huang, *J. Power Sources* 216 (2012) 131–138.
- [8] S.P.V. Nadimpalli, V.A. Sethuraman, S. Dalavi, B. Lucht, M.J. Chon, V.B. Shenoy, P.R. Guduru, *J. Power Sources* 215 (2012) 145–151.
- [9] J.L. Goldman, B.R. Long, A.A. Gewirth, R.G. Nuzzo, *Adv. Funct. Mater.* 21 (2011) 2412–2422.
- [10] R. Yi, F. Dai, M.L. Gordin, S.R. Chen, D.H. Wang, *Adv. Energy Mater.* 3 (2013) 295–300.
- [11] C.K. Chan, R. Ruffo, S.S. Hong, Y. Cui, *J. Power Sources* 189 (2009) 1132–1140.
- [12] A.M. Glass, K. Nassau, *J. Appl. Phys.* 51 (1980) 3756–3761.
- [13] N. Ding, J. Xu, Y.X. Yao, G. Wegner, X. Fang, C.H. Chen, I. Lieberwirth, *Solid State Ionics* 180 (2009) 222–225.
- [14] L.F. Shen, X.G. Zhang, H.S. Li, C.Z. Yuan, G.Z. Cao, *J. Phys. Chem. Lett.* 2 (2011) 3096–3101.
- [15] H. Yildirim, J.P. Greeley, S.K.R.S. Sankaranarayanan, *PCCP* 14 (2012) 4565–4576.
- [16] G.V. Samsonov, *The Oxide Handbook*, second ed., IFI/Plenum, New York, 1982.
- [17] J. Cho, Y.J. Kim, T.J. Kim, B. Park, *Angew. Chem. Int. Ed.* 40 (2001) 3367–3369.
- [18] M. Tanaka, K. Higashida, H. Nakashima, H. Takagi, M. . Fujiwara, *Int. J. Fract.* 139 (2006) 383–394.
- [19] www.azom.com/ 2013. (article ID = 1114, accessed 15.08.13).
- [20] X.C. Xiao, P. Lu, D. Ahn, *Adv. Mater.* 23 (2011) 3911.
- [21] Y. He, X.Q. Yu, Y.H. Wang, H. Li, X.J. Huang, *Adv. Mater.* 23 (2011) 4938–4941.
- [22] Q. Shao, L.F. Voss, A.M. Conway, R.J. Nikolic, M.A. Dar, C.L. Cheung, *Appl. Phys. Lett.* 102 (2013) 063505.
- [23] S.M. George, *Chem. Rev.* 110 (2010) 111–131.
- [24] J. Aarik, A. Aidla, H. Mandar, T. Uustare, *Appl. Surf. Sci.* 172 (2001) 148–158.
- [25] S. Ghosal, T.F. Baumann, J.S. King, S.O. Kucheyev, Y.M. Wang, M.A. Worsley, J. Biener, S.F. Bent, A.V. Hamza, *Chem. Mater.* 21 (2009) 1989–1992.
- [26] M.D. Groner, F.H. Fabreguette, J.W. Elam, S.M. George, *Chem. Mater.* 16 (2004) 639–645.
- [27] P. Limthongkul, Y.I. Jang, N.J. Dudney, Y.M. Chiang, *Acta Mater.* 51 (2003) 1103–1113.
- [28] X.H. Liu, L.Q. Zhang, L. Zhong, Y. Liu, H. Zheng, J.W. Wang, J.H. Cho, S.A. Dayeh, S.T. Picraux, J.P. Sullivan, S.X. Mao, Z.Z. Ye, J.Y. Huang, *Nano Lett.* 11 (2011) 2251–2258.
- [29] U. Gosele, K.N. Tu, *J. Appl. Phys.* 53 (1982) 3252–3260.
- [30] Z.W. Cui, F. Gao, J.M. Qu, *J. Mech. Phys. Solids* 61 (2013) 293–310.
- [31] Y.H. An, H. Jiang, *Modell. Simul. Mater. Sci. Eng.* (2013) in press.
- [32] C.F. Herrmann, F.W. DelRio, S.M. George, V.M. Bright, *Proc. SPIE* 5715 (2005) 159–166.
- [33] O. Anderson, C.R. Ottermann, R. Kuschnerit, P. Hess, K. Bange, Fresenius' *J. Anal. Chem.* 358 (1997) 290–293.
- [34] M.A. Hopcroft, W.D. Nix, T.W. Kenny, *J. MEMS* 19 (2010) 229–238.
- [35] J.J. Wortman, R.A. Evans, *J. Appl. Phys.* 36 (1965) 153.
- [36] B. Hertzberg, J. Benson, G. Yushin, *Electrochem. Commun.* 13 (2011) 818–821.
- [37] M.J. Chon, V.A. Sethuraman, A. McCormick, V. Srinivasan, P.R. Guduru, *Phys. Rev. Lett.* 107 (2011) 045503.
- [38] X.H. Liu, H. Zheng, L. Zhong, S. Huan, K. Karki, L.Q. Zhang, Y. Liu, A. Kushima, W.T. Liang, J.W. Wang, J.H. Cho, E. Epstein, S.A. Dayeh, S.T. Picraux, T. Zhu, J. Li, J.P. Sullivan, J. Cumings, C.S. Wang, S.X. Mao, Z.Z. Ye, S.L. Zhang, J.Y. Huang, *Nano Lett.* 11 (2011) 3312–3318.
- [39] H. Yang, S. Huang, X. Huang, F.F. Fan, W.T. Liang, X.H. Liu, L.Q. Chen, J.Y. Huang, J. Li, T. Zhu, S.L. Zhang, *Nano Lett.* 12 (2012) 1953–1958.
- [40] M.T. McDowell, I. Ryu, S.W. Lee, C.M. Wang, W.D. Nix, Y. Cui, *Adv. Mater.* 24 (2012) 6034.
- [41] X.H. Liu, F.F. Fan, H. Yang, S.L. Zhang, J.Y. Huang, T. Zhu, *ACS Nano* 7 (2013) 1495–1503.
- [42] M. Pharr, K.J. Zhao, X.W. Wang, Z.G. Suo, J.J. Vlassak, *Nano Lett.* 12 (2012) 5039–5047.